

# Critical Surface for Explosions of Rotational Core-Collapse Supernovae

Wakana Iwakami

Yukawa Institute for Theoretical Physics, Kyoto University, Oiwake-cho, Kitashirakawa,  
Sakyo-ku, Kyoto, 606-8502, Japan

Advanced Research Institute for Science and Engineering, Waseda University, 3-4-1,  
Okubo, Shinjuku, Tokyo, 169-8555, Japan

Hiroki Nagakura

Yukawa Institute for Theoretical Physics, Kyoto University, Oiwake-cho, Kitashirakawa,  
Sakyo-ku, Kyoto, 606-8502, Japan

and

Shoichi Yamada

Advanced Research Institute for Science and Engineering, Waseda University, 3-4-1,  
Okubo, Shinjuku, Tokyo, 169-8555, Japan

wakana@heap.phys.waseda.ac.jp

Received \_\_\_\_\_; accepted \_\_\_\_\_

## ABSTRACT

The effect of rotation on the explosion of core-collapse supernovae is investigated systematically in three-dimensional simulations. In order to obtain the critical conditions for explosion as a function of mass accretion rate, neutrino luminosity, and specific angular momentum, rigidly rotating matter was injected from the outer boundary with angular momentum increased every 500 ms. It is found that there is a critical value of the specific angular momentum, above which the standing shock wave revives, for a given combination of mass accretion rate and neutrino luminosity. The explosion can occur by rotation even if the neutrino luminosity is lower than the critical value for a given mass accretion rate in the non-rotation models. The coupling of rotation and hydrodynamical instabilities plays an important role to characterize the dynamics of shock revival within the range of realistic specific angular momentum. Contrary to expectations from past studies, the most rapidly expanding direction of the shock wave is not along the rotation axis. Being perpendicular to the rotation axis on average, it wobbles in various directions. Its dispersion is small when the spiral mode of the standing accretion shock instability (SASI) governs the dynamics, while it is large when neutrino-driven convection is dominant. Comparing 2D and 3D rotation models, we found that  $m \neq 0$  modes of convection or SASI are important for shock revival around the critical surface.

*Subject headings:* supernovae — hydrodynamics — instabilities — rotation

## 1. INTRODUCTION

A number of observational results and numerical studies on core-collapse supernovae have indicated that multi-dimensional effects are important in their explosions. Observations have revealed that the explosions are asymmetric (e.g., Wang et al. 2001; Leonard et al. 2006), and one-dimensional (1D) simulations have shown that the explosions do not reproduce, except for low mass progenitors (e.g., Liebendörfer et al. 2005; Sumiyoshi et al. 2005). Hence, a large number of multi-dimensional numerical studies have been done to investigate the association of hydrodynamical instabilities, rotation, and magnetic fields with the explosions (see Janka 2012; Burrows 2013, for latest reviews). In this paper, we discuss the effects of rotation on shock revival with hydrodynamical instabilities.

Two hydrodynamical instabilities: neutrino-driven convection and the standing accretion shock instability (SASI), can appear before shock revival. Convection is developed behind the shock wave by neutrino heating, if there is enough time to grow until matter gets out of the gain region to be accreted onto the proto-neutron star (PNS) (Foglizzo et al. 2006). Both two-dimensional (2D) and three-dimensional (3D) simulations of core-collapse supernovae have confirmed the dominance of convection (e.g., Herant et al. 1992; Burrows et al. 1992; Janka 1996; Fryer & Warren 2002; Nordhaus et al. 2010; Couch 2013; Dolence 2013; Murphy et al. 2013; Ott et al. 2013). On the other hand, SASI is the instability of shock wave deformations (Foglizzo et al. 2007). The low modes of shock geometry make coherent flow structures behind the shock wave, whereas neutrino-driven convection generates turbulent flows in the gain region. Numerical studies on SASI have been done by 2D and 3D simulations (e.g., Blondin et al. 2003; Ohnishi et al. 2006; Burrows et al. 2006; Blondin & Mezzacappa 2007; Iwakami et al. 2008a; Scheck et al. 2008; Fernández 2010; Burrows 2012; Takiwaki et al. 2012; Wongwathanarat et al. 2013; Hanke et al. 2012, 2013), linear analyses (e.g., Foglizzo et al. 2007; Yamasaki & Yamada

2007; Yamasaki & Foglizzo 2008; Foglizzo et al. 2009; Fernández & Thompson 2009b; Guilet et al. 2010, 2012), and SWASI experiment (Foglizzo et al. 2012).

Recently, we have presented the parametric study of flow patterns by 3D simulations (Iwakami et al. 2014), and investigated which convection or SASI is more dominant before shock revival. Depending on mass accretion rate and neutrino luminosity, either of them grows regardless of whether explosion occurs or not. Convection tends to be dominant for low mass accretion rates and high neutrino luminosities, and SASI appears as the mass accretion rate increases and the neutrino luminosity decreases. Then, we have calculated  $\chi$  parameter, Our results have shown that convection takes place behind the shock wave for  $\chi > 3$ , while SASI occurs for  $\chi < 3$ , being consistent with the theoretical prediction (Foglizzo et al. 2006). Furthermore, intermediate states between convection and SASI can be observed in the nonlinear phase around  $\chi \sim 3$ . On the basis of these results, we are interested in the effect of rotation on the hydrodynamical instabilities and shock revival.

Observational data have implicated that main-sequence massive stars, which can be progenitors of core-collapse supernovae, can rotate as the sun (Tassoul 1978). Hence, the effect of rotation on the core-collapse supernovae have been investigated by 2D axisymmetric simulations. Although non-spherically symmetric structures of rotating stars can explain the results of observations on the matter mixing in SN1987A (e.g. Chevalier 1989; Yamada & Sato 1990, 1991), rotation has a negative effect on prompt explosion mechanism (e.g. Müller and Hillebrandt 1981; Yamada & Sato 1994; Fryer & Heger 2000). The centrifugal force prevents the iron core from contracting, and less gravitational energy leads to weak explosions. On the other hand, in the context of delayed explosion mechanism, the enhancement of neutrino heating near the rotation axis can induce a jet-like explosion (Kotake et al. 2003). The analytical study, considering neutrino heating and cooling with realistic equation of state (EOS), have also indicated the shock revival

firstly takes place at the rotation axis, because the lack of a steady solution is estimated to begin from the rotation axis (Yamasaki & Yamada 2005). The rotation-induced neutrino heating anisotropy, however, could not be a crucial factor in the explosion, which have been concluded by 2D numerical studies (Buras et al. 2003; Walder et al. 2005). Some 3D numerical studies for rotation models have been done so far, for example, Fryer & Warren (2004) has presented the results of core-collapse simulations of rotating stars by using the 3D smoothed particle hydrodynamics (SPH) code, Iwakami et al. (2009a,b) have investigated the effect of rotation on SASI by using the 3D Eulerian hydrodynamics code, and Nakamura et al. (2014) has recently performed 3D simulations with  $15M_{\odot}$  progenitors. However, it has not been well-understood how rotation affects the shock revival under the non-axisymmetric hydrodynamical instabilities developed. In this paper, we investigate it in a systematic manner with 3D hydrodynamical simulations with light-bulb approximation for neutrino heating and cooling.

The organization of this paper is as follows. Models and numerical setups are described in Section 2, results in Section 3, and conclusion in Section 4.

## 2. Models and Numerical Setups

An explosion of a core-collapse supernova has a lot of stages. In this paper, we focus only on the shock revival after the core bounce. A computational domain covers the inner part of the iron core, where the spherical coordinate system  $(r, \theta, \phi)$  is considered. The central part, corresponding to PNS, is excised from the computational domain. The initial flows are the 1D steady solutions (Yamasaki & Yamada 2006). The matter is accreted from the outer boundary onto the PNS with a fixed mass accretion rate, and a spherical shock wave is stalled on its way. The neutrino spheres, being assumed to be inside the PNS, isotropically give off neutrinos with a fixed neutrino flux to the optically thin matter. More

details about the initial and boundary conditions are described in our previous paper for non-rotation models (Iwakami et al. 2014). The amplitude of the initial perturbation of radial velocity  $\delta v_r/v_r$  is determined at random in every cell within 1%.

The basic equations are the three-dimensional compressible Euler equations (Iwakami et al. 2008a). Thermodynamical variables are obtained from Shen’s EOS (Shen et al. 1998). The light bulb approximation is implemented to calculate the neutrino heating/cooling term (Ohnishi et al. 2006). These equations are numerically solved with ZEUS-MP/2 code (Hayes et al. 2006). Tensor-type artificial viscosity is used for suppressing the carbuncle phenomenon around the polar axis (Iwakami et al. 2008a,b). The computational region, defined from  $r_{\text{in}}$  to  $r_{\text{out}}$  on the entire solid angle, is divided into  $300 \times 30 \times 60$  grid cells, where  $r_{\text{in}}$  and  $r_{\text{out}}$  are the inner and outer boundaries in the radial direction. The radial resolution is determined to be 1% of the radius everywhere, and the azimuthal resolution is adjusted to be exactly same spacings in order not to cause any numerical oscillations around the polar axis. The temperatures of electron-type neutrinos and anti-neutrinos are set to be the typical values in the post-bounce phase,  $T_{\nu_e} = 4$  MeV and  $T_{\bar{\nu}_e} = 5$  MeV, respectively. The mass of the PNS is fixed to be  $M_{\text{PNS}} = 1.4M_{\odot}$ . The range of neutrino luminosities is  $L_{\nu} = 2.0 - 6.0 \times 10^{52}$  erg s<sup>-1</sup>, and that of mass accretion rates is  $\dot{M} = 0.25 - 1.0 M_{\odot}$  s<sup>-1</sup>. These parameters of all models are summarized in Table 1.

In this study, rigidly rotating matter is injected from the outer boundary into the computational region with angular momentum increased every 500 ms. The azimuthal velocity imposed on the outer boundary is written in

$$v_{\phi}(r_{\text{out}}, \theta) = \beta \times 10^8 \times \left( \frac{10^8}{r_{\text{out}}} \right) \times \sin \theta \text{ [cm s}^{-1}\text{]}, \quad (1)$$

where  $\beta$  is a parameter of rotation. The detailed derivation of Eq. (1) and its validity can be referred to Appendix A. The corresponding specific equatorial angular momentum is

described as

$$L = \beta \times 10^{16} [\text{cm}^2 \text{ s}^{-1}]. \quad (2)$$

According to Heger et al. (2000, 2005), the  $15 M_{\odot}$  pre-SN star has  $L \sim 10^{14} - 10^{15} \text{ cm}^2 \text{ s}^{-1}$  with magnetic fields and  $L \sim 10^{16} - 10^{17} \text{ cm}^2 \text{ s}^{-1}$  without ones, in the range of the enclosed mass from  $1.4M_{\odot}$  to  $2.5M_{\odot}$ . In this paper, the range of  $\beta$  is taken from 0.0 to 1.0, and  $\beta$  is called the normalized specific angular momentum.

### 3. RESULTS AND DISCUSSIONS

#### 3.1. Critical Surface for Explosion

Burrows & Goshy (1993) have discovered that there is a critical neutrino luminosity  $L_{\nu}$ , above which there is no steady solution, for a given mass accretion rate  $\dot{M}$ . A critical curve, dividing the parameter space into explosion and non-explosion areas, can be depicted in the  $L_{\nu} - \dot{M}$  plane. In this study, we add one more parameter, a normalized specific angular momentum  $\beta$ , to  $L_{\nu}$  and  $\dot{M}$ . Then we draw a critical surface, above which the shock wave keep propagating outward at least up to 500 km, in the three-dimensional parameter space with  $\dot{M}$ ,  $L_{\nu}$  and  $\beta$  axes in Figure 1. In order to obtain the critical surface in Figure 1, rigidly rotating matter is injected from the outer boundary into the supersonic flow with specific angular momentum increased every 500 ms. It is found that there is a critical value of  $\beta$  for a given combination of  $\dot{M}$  and  $L_{\nu}$ , represented by the monochrome boxes in Figure 1. The more rapidly rotating the matter is, the lower neutrino luminosity the shock revival requires. The green lines, connected with the black squares on the plane at  $\beta = 0.0$ , can be considered as the critical curve for non-rotation models, and the critical curve moves toward low  $L_{\nu}$  as  $\beta$  increases. Therefore, it is confirmed that the rotation makes easy to explode in the 3D models. Here, we notify that the critical curve at  $\beta = 0.0$  is located at

somewhat higher  $L_\nu$  than the curve given by more realistic simulations (Nordhaus et al. 2010; Hanke et al. 2012; Couch 2013), although it agrees well with the curve obtained from the analytical study, taking convection into account, in the almost same setups as ours (Yamasaki & Yamada 2006). Hence, it is estimated that the critical surface, given by more sophisticated simulations, moves toward lower  $L_\nu$  than the surface obtained in this study.

The time evolutions of the shock radius are presented in Figure 2, calculated with the expansion coefficient  $c_0^0$  in Equation (B4) multiplied by  $K_0^0$  in Equation (B3). Rotation makes the shock radius enlarged, and more rapid rotation causes shock revival even if the neutrino luminosity is not enough large to induce shock revival for non-rotation models. The behaviors of the shock oscillation in the slow-rotation models for  $\beta \lesssim 0.4$  are reflected the features of the flow pattern developed behind the shock wave for non-rotation models. In our previous study, the flow pattern is classified into sloshing motion (SL), spiral motion (SP), high-entropy bubbles (BB), spiral motion with rising buoyant bubbles (SPB), and spiral motion with pulsating rotational velocity (SPP). The SL and SP are caused by the growth of SASI, and BB is resulted in the development of convection. The last two patterns are considered as intermediate patterns of SP and BB. The abbreviated expressions of these patterns for non-rotation models are written in the bottom-right corners of the panels in Figure 2. More detailed characteristics of these non-rotation models are described in our previous paper (Iwakami et al. 2014), except for Model B, whose non-rotation properties are summarized in Appendix D in this paper.

Figure 3 shows the time evolutions of the net heating rate, integrated behind the shock wave, for all models. It is clear that the time variations of them are correlated with those of the shock radius in Figure 2. Therefore, the neutrino heating mechanism is considered to work predominantly for the shock revival at least within the range of  $\beta$  from 0.0 to 1.0. As the speed of rotation is amplified, the net heating rates tend to increase with



growing the shock radii. Hence, it is obvious that the enhancement of neutrino heating can involve the rotation. Figure 4 shows the time evolutions of the angular momentum in the polar direction, integrated behind the shock wave. The matter behind the shock wave has the angular momentum, which rotates in the same direction as the injected matter. The angular momentum behind the shock wave is proportional to  $\beta$  for the early phases, and it exponentially increases before shock revival. Such amplifications of the angular momentum behind the shock wave can induce the strong centrifugal force to the shocked matter, and they are supposed to change the dynamics of flow and the neutrino heating/cooling of matter.

The two possibilities, how the shock revival can occur in the rotating cores, are considered here. One is prolate explosion: shock expansion begins from the rotation axis at the onset of the explosion (Yamasaki & Yamada 2005). The other is oblate explosion: the preferred direction of explosion is perpendicular to the rotation axis (Nakamura et al. 2014). In the next section, we focus on the expanding direction of the shock wave at the shock revival.

### 3.2. Expanding Direction of a Shock Wave at Shock Revival

Figure 5 presents the snapshots of the entropy contour maps in the meridian plane at  $\phi = 0$  for explosion models, when the average shock radii reach 300 km after shock revival. The left, middle, and right three panels show the entropy distributions for explosion models with rapid-rotation, slow-rotation, and non-rotation, respectively. The shock expansions have a strong unipolar nature in the two rapid-rotation models (Figure 5 (a) and (d)), and it has a dipolar nature in the other rapid rotation one (Figure 5 (g)). On the other hand, such directional characteristics are not clear in the non-rotation models, since high entropy regions are formed in various directions (Figure 5 (c), (f), (i)). In the slow-rotation

models, the weak unipolar explosions can be observed (Figure 5 (b), (e), and (h)). Although several realizations should be investigated for each model in order to confirm whether these directional properties are robust, it is obvious that the expanding directions of the shock waves are not specified along the polar axis nor the equatorial plane within the range of  $\beta$  from 0.1 to 1.0.

The time evolutions of the polar angles of the direction in the maximum shock radius for all models are shown in Figure 6. The black lines correspond to the results for non-rotation models, and the characteristics of them depend on the dominant flow patterns in the nonlinear phase (Iwakami et al. 2014). Once a rotational flow passes through the shock wave, the rotation axis of the flow behind the shock wave is fixed to be parallel to the polar axis in any flow patterns, and the orientation in the maximum shock radius prefers to be perpendicular to the polar axis due to the centrifugal force. Especially, the variance of  $\theta$  from  $90^\circ$  is small in  $\beta < 6$  when spiral SASI is dominant for Models D and G, while it is large when buoyant bubbles are generated by neutrino-driven convection for Models B and E. If the intermediate patterns between SASI and convection appear in the non-rotation models, the variances have medium values for Models A and H. The emergence of many buoyant bubbles prevents the global rotation of matter in the gain region, and the centrifugal force, acting on the matter toward perpendicular to the polar axis, can be reduced. Furthermore, for Models D and G, the expanding direction of the shock wave are abruptly unstable as  $\beta$  increases. Eventually, the directions of shock revival, indicated at the right end points of the lines, are not confined neither along the rotation axis nor along the equatorial plane.

Why does the expanding direction for Models D and G become unstable with increasing specific angular momentum? To answer the question, we present  $\bar{\chi}$  as a function of  $\beta$  for non-explosion models in Figure 7. The parameter  $\chi$ , the ratio of advection time to

growth time of convection, is a good indicator of the emergence of the buoyant bubbles by neutrino-driven convection, and its criterion is  $\chi > 3$  (Foglizzo et al. 2006). In this study, we calculate  $\bar{\chi}$  at each  $\beta$ .  $\bar{\chi}$  is obtained from the angle-averaged mean flow of the quasi-periodic state, and the details about how to calculate  $\bar{\chi}$  are described in Appendix C. Although the intermediate patterns of spiral motion with buoyant bubbles exists around  $\bar{\chi} \sim 3.5$  and pulsating spiral motion around  $\bar{\chi} \sim 2.5$ , we obtain the result that buoyant bubbles emerge in the gain region if  $\bar{\chi} > 3$ . Hence, we call the region above and below  $\bar{\chi} = 3$  the convection and SASI regions, respectively. Models D and G exist in the SASI region at  $\beta = 0$ . However, each  $\bar{\chi}$  grows with increasing  $\beta$ , and exceeds the line of  $\bar{\chi} = 3$  at  $\beta = 0.7$  for Model D and at  $\beta = 0.8$  for Model G. The values of  $\beta$  agree with the ones, at which the orientations directed in the maximum shock radius become unstable (Figure 6 (d) and (g)). Here, we consider that the rapid rotation changes the flow dynamics for Model D and G: the dominant instability is changed from SASI to convection by rotation. The rapid rotation can induce the large centrifugal force, which can more effectively act on the flow with spiral motion than it with buoyant bubbles. As a result, the shock wave is enlarged. The larger the shock radius is, the longer the advection time tend to be. Therefore, they can acquire enough time to grow buoyant bubbles, and the expanding directions become unstable. In contrast, within the quasi-periodic state, Models A, B, H and E keep in the same region as they initially reside in, even if  $\beta$  increases. This is the reason why the characteristics of the time evolutions of the expanding direction do not significantly changed (Figure 6 (a), (b), (e), and (h)).

Finally, we refer to the difference between 2D and 3D. The time evolution of the averaged shock radius in 2D and 3D simulations for  $\dot{M} = 0.6M_{\odot}$  and  $1.0M_{\odot}$  is shown in Figure 8. There are three phases: the 2D models without rotation from  $t = 0$  to  $0.5$  s, the 2D models with rotation from  $t = 0.5$  to  $1.5$  s, and the 3D models with rotation from  $t = 1.5$  to  $2.0$  s. We found that the explosions occur only in the 3D models at the parameters on

the critical surface. This means that  $m \neq 0$  modes of convection or SASI play an important role for rotational explosions at least around the critical surface. The centrifugal force, acting on the fragmented matter by hydrodynamical instability, further deforms the shock wave and enhance the neutrino heating behind the shock wave. It is also confirmed in more realistic simulations by other groups that 3D models with rotation is easier to explode than 2D (Nakamura et al. 2014, T. Takiwaki, private communication), but it has a possibility to depend on the parameters such as a rotation rate. In order to clarify the whole picture of this topic, more 3D parametric studies at the different parameters are interesting, and its detailed mechanism should be investigated by more realistic simulation with higher resolution.

#### 4. SUMMARIES AND DISCUSSIONS

In this paper, we investigated how rotation affects the shock revival for core-collapse supernovae under the situations in which non-axisymmetric hydrodynamical instabilities are developed. In order to obtain a critical surface, above which the shock wave can run away, in the three-dimensional parameter space  $(\dot{M}, L_\nu, \beta)$ , the rotating matter is injected from the outer boundary into the supersonic flow with increasing  $\beta$  every 500 ms, where  $\dot{M}$ ,  $L_\nu$ ,  $\beta$  are the mass accretion rate, the neutrino luminosity, and the normalized specific angular momentum, respectively. Based on the results by Heger et al. (2005), the range of the specific angular momentum is taken to be  $10^{15} - 10^{16} \text{ cm}^2 \text{ s}^{-1}$  in this study.

We found that: (1) there is a critical value of  $\beta$  for a given combination of  $\dot{M}$  and  $L_\nu$ , (2) rotation makes a stalled shock wave easier to revive under the development of the three-dimensional hydrodynamical instabilities, (3) the neutrino heating mechanism works within the range of the specific angular momentum of  $10^{15} - 10^{16}$ , (4) the expanding direction of the shock wave tend to be perpendicular to the rotation axis, (5) the

dispersion of the expanding direction from the equatorial plane depends on the dominant hydrodynamical instability of SASI and convection, (6) the rapid rotation can change the dominant instability from SASI to convection, (7)  $m \neq 0$  modes play an important role to the rotational explosions.

From (4) and (5), we estimate that the probability distribution of the expanding direction at shock revival depends on the dominant hydrodynamical instability within the range of the given specific angular momentum. Its dispersion is small for SASI and is large for convection, while the average is common in the direction perpendicular to the rotation axis. In this study, the convection is more dominant than SASI at the shock revival due to (6), but the dominant instabilities might be different from this study in the different parameters. Furthermore, if the time scale of expanding shock waves by strong rotation is shorter than the growth time of these instabilities, the expanding direction might change from around the equatorial plane to the rotation axis. Hence, the survey of the broader range of the parameters ( $L_\nu$ ,  $\dot{M}$ ,  $\beta$ ) with a large number of realizations is interesting to understand the overall picture of the explosion of the rotating stars.

In this study we assumed to be a constant mass accretion rate, a constant proto-neutron star mass, and a constant neutrino luminosity. The initial condition is the steady solutions with a random perturbation. Hence, the results should be confirmed in the context of the dynamical evolutions of the actual profiles of the supernova progenitors. Moreover, the results should be also validated with more accurate treatment of neutrino transfer, which will be addressed by using Boltzmann solver for neutrino radiation hydrodynamics (Sumiyoshi et al. 2014; Nagakura et al. 2014). It is also interesting to know the neutrino signal and gravitational wave originated from the rotating matter behind the shock wave. These problems should be investigated in the future work.

Numerical computations were performed on the XC30 and the general common use

computer system at the center for the Computational Astrophysics, CfCA, the National Astronomical Observatory of Japan, as well as, the Altix UV 1000 at the IFS in Tohoku University and SR16000 at YITP in Kyoto University. This study was supported by the Grants-in-Aid for the Scientific Research (NoS. 24244036, 24740165), the Grants-in-Aid for the Scientific Research on Innovative Areas, "New Development in Astrophysics through multi messenger observations of gravitational wave sources" (No. 24103006), and the HPCI Strategic Program from the Ministry of Education, Culture, Sports, Science and Technology (MEXT) in Japan.

### A. Formulation for Rotational Velocity

The mass accretion rate is written in

$$\dot{M}(r) \equiv \int_0^{4\pi} \rho v_r r^2 d\Omega, \quad (\text{A1})$$

and the angular momentum passing through the spherical boundary per unit time is described as

$$i_z(r) \equiv \int_0^{4\pi} \rho v_r (v_\phi r \sin \theta) r^2 d\Omega, \quad (\text{A2})$$

where  $\rho$ ,  $v_r$ ,  $v_\theta$ , and  $\Omega$  are the density, radial velocity, azimuthal velocity, and solid angle, respectively. In the rigid rotation, the azimuthal velocity is defined as

$$v_\phi(r, \theta) = r \sin \theta \omega_z(r), \quad (\text{A3})$$

where  $\omega_z$  is the angular velocity of rotation around the polar axis. If we assume the steady and spherically symmetric distributions of density and radial velocity in the supersonic flow above the shock wave, the angular momentum rate can be written in

$$i_z = \frac{2}{3} \dot{M} r^2 \omega_z(r), \quad (\text{A4})$$

where  $\dot{l}_z$  and  $\dot{M}$  are constant along the radial direction because of the angular momentum and mass conservation laws. Therefore,

$$r^2 \omega_z(r) = C, \quad (\text{A5})$$

where  $C$  is a constant. Then, Eq. (A3) is

$$v_\phi(r, \theta) = \frac{C}{r} \sin \theta. \quad (\text{A6})$$

Here we set to be  $C = \beta \times 10^6$  so that the angular velocity is  $\beta$  rad s<sup>-1</sup> at 1000 km.

In order to confirm the validity of the assumptions described above near the outer boundary, the radial distributions of the time- and angle-averaged azimuthal velocity  $\bar{v}_\phi$  for non-explosion models are shown in Fig. 9. The right endpoints of the lines correspond to the outer boundaries, and the dashed line at  $\bar{r}_{sh}$  indicate the maximum shock radius of all models. The lines having same  $\beta$  are overlapped each other for  $\bar{r}_{sh} \ll r$ , while the lines are deviated from one another for  $r \lesssim \bar{r}_{sh}$ . Therefore, the angular velocity is appropriately given to the flow even if the outer boundaries are different depending on the models.

## B. Average Shock Radius and Mode Analysis

The distance of the shock front from the origin can be written in a linear combination of the spherical harmonic components,

$$R_{sh}(\theta, \phi, t) = \sum_{l=0}^{\infty} \sum_{m=-l}^l c_l^m(t) Y_l^m(\theta, \phi), \quad (\text{B1})$$

where  $Y_l^m$  is expressed by the associated Legendre polynomial  $P_l^m$  as

$$Y_l^m = K_l^m P_l^m(\cos \theta) e^{im\phi}, \quad (\text{B2})$$

$$K_l^m = \sqrt{\frac{2l+1}{4\pi} \frac{(l-m)!}{(l+m)!}}. \quad (\text{B3})$$

The expansion coefficients are described as

$$c_l^m(t) = \int_0^{2\pi} d\phi \int_0^\pi d\theta \sin \theta R_{\text{sh}}(\theta, \phi, t) Y_l^{m*}(\theta, \phi), \quad (\text{B4})$$

where the superscript  $*$  denotes complex conjugation.

The following quantities:

$$A_l(t) = \sqrt{\sum_{m=-l}^l |c_l^m(t)/c_0^0(t)|^2}, \quad (\text{B5})$$

$$A_{1,2}(t) = \sqrt{\sum_{l=1}^2 \sum_{m=-l}^l |c_l^m(t)/c_0^0(t)|^2}, \quad (\text{B6})$$

$$A_{4,5}(t) = \sqrt{\sum_{l=4}^5 \sum_{m=-l}^l |c_l^m(t)/c_0^0(t)|^2}, \quad (\text{B7})$$

and their time-averages:

$$\bar{A}_l = \frac{1}{T} \int_{t_s}^{t_e} A_l(t) dt, \quad (\text{B8})$$

$$\bar{A}_{1,2} = \frac{1}{T} \int_{t_s}^{t_e} A_{1,2}(t) dt, \quad (\text{B9})$$

$$\bar{A}_{4,5} = \frac{1}{T} \int_{t_s}^{t_e} A_{4,5}(t) dt, \quad (\text{B10})$$

are used for the mode analysis, where  $T = t_e - t_s$  is the integral time,  $t_s$  is the starting time, and  $t_e$  is the ending time for integration.

### C. $\chi$ Parameter

Taken the effect of advection into account (Foglizzo et al. 2006),  $\chi$  parameter gives for the new criterion of convective instability, which is the ratio of advection time to growth time of buoyancy, is defined as

$$\chi \equiv \int_{r_{\text{gain}}}^{r_{\text{sh}}} \left| \frac{N}{u_r} \right| dr, \quad (\text{C1})$$

where  $r_{\text{gain}}$  is the gain radius,  $r_{\text{sh}}$  is the shock radius, and  $u_r$  is the radial velocity. The

Brunt-Väisälä frequency  $N$  is can be written in

$$N^2 = \left| \frac{1}{\Gamma_1 p} \frac{dp}{dr} - \frac{1}{\rho} \frac{d\rho}{dr} \right| g, \quad (\text{C2})$$



$$\Gamma_1 = \left( \frac{\partial \ln p}{\partial \ln \rho} \right)_{S, Y_e}, \quad (\text{C3})$$

where  $p$ ,  $\rho$ ,  $S$ ,  $Y_e$ , and  $g$  are the pressure, density, entropy, electron fraction, and gravitational acceleration, respectively. The gravitational acceleration is given approximately in the gain region as  $g = \frac{GM_{\text{PNS}}}{r^2}$ , in which  $M_{\text{PNS}}$  and  $G$  is the PNS mass and the gravitational constant.

Furthermore, for three-dimensional quasi-steady models, we define the angle-averaged mean flow, where the quantities are averaged over the solid angle and from the onset of the quasi-steady state to the end of computation,

$$\bar{q}_{1\text{D}}(r) = \frac{1}{4\pi} \int_0^{4\pi} \left[ \frac{1}{T} \int_{t_s}^{t_e} q(r, \theta, \phi, t) dt \right] d\Omega. \quad (\text{C4})$$

where  $q(r, \theta, \phi, t)$  is an arbitrary quantity (i.e.,  $\rho$ ,  $u_r$ , and so on),  $t_s$  is the beginning time of the quasi-steady state, and  $t_e$  is the ending time of the computation. The parameter  $\bar{\chi}_{1\text{D}}$  is then obtained as

$$\bar{\chi}_{1\text{D}} = \int_{\bar{r}_{\text{gain1D}}}^{\bar{r}_{\text{sh1D}}} \left| \frac{\bar{N}_{1\text{D}}(r)}{\bar{u}_{r1\text{D}}(r)} \right| dr, \quad (\text{C5})$$

$$\bar{N}_{1\text{D}}^2 = \left| \frac{1}{\bar{\Gamma}_{11\text{D}} \bar{p}_{1\text{D}}} \frac{d\bar{p}_{1\text{D}}}{dr} - \frac{1}{\bar{\rho}_{1\text{D}}} \frac{d\bar{\rho}_{1\text{D}}}{dr} \right| g, \quad (\text{C6})$$

where the quantities with a bar involves the angle-averaged mean flow. The thermodynamical variables,  $\bar{p}_{1\text{D}}$  and  $\bar{\Gamma}_{11\text{D}}$ , are given by an EOS table as a function of  $\bar{\rho}_{1\text{D}}$ ,  $\bar{e}_{1\text{D}}$  and  $\bar{Y}_{e1\text{D}}$ .  $\bar{r}_{\text{gain1D}}$  is the gain radius where the net heating rate of the angle-averaged mean flow is equal to zero, and  $\bar{r}_{\text{sh1D}}$  is the shock radius where  $\bar{S}$  is equal to 3.1.

## D. Model B

The characteristics of a non-rotation model for  $\dot{M} = 0.2M_{\odot}$  and  $L_{\nu} = 2.75 \times 10^{52}$  erg s<sup>-1</sup>, called model B, are summarized in this appendix. The semi-nonlinear/nonlinear flow patterns and physical parameters are listed in Table 2, and the time evolutions of normalized mode amplitudes, the orientations of the rotation axis, and the magnitudes of

angular momentum are shown in Figure 10, where mode amplitudes and  $\chi$  parameter are defined in Appendix B and C, respectively. We found that both SP (Figure 10(a)) and BB (Figure 10(b)) appear in the semi-nonlinear phase, depending on the initial random perturbations in the different seed of random number. The oscillated and monotonic growth of mode amplitudes indicates the dominance of spiral motions and buoyant bubbles, respectively. The parameter  $\chi$  is 4.1, which might be a critical value divided into SASI-dominant region and convection-dominant one in the semi-nonlinear phase in our simulations. In the nonlinear phase, the flow pattern turns into BB for both models, judged from the unstable behavior of the rotation axis (Figure 10 (d), (e)) and the low angular momentum (Figure 10 (g), (h)), where  $\bar{\chi}$  is about 5.0. Furthermore, we have done the resolution test for Model B. Flow pattern in the higher resolution models are consistent with one in the lower resolution models. In the semi-nonlinear phase, BB emerges in the middle resolution model (left panel in Fig. 10(c)), and SP appears in the higher resolution model (right panel in Fig. 10(c)). In the nonlinear phase, BB can be seen in both middle and higher resolution models. Although the ratio of mode amplitudes  $\bar{A}_{l=1,2}/\bar{A}_{l=4,5}$  decrease with increasing resolution, there is no problem to identify the flow pattern, which is discussed in Iwakami et al. (2014).

## REFERENCES

- Blondin, J. M., Mezzacappa, A., & DeMarino, C. 2003, *ApJ*, 584, 971
- Blondin, J. M., & Mezzacappa, A., 2007, *Nature*, 445, 58
- Burrows, A. & Fryxell, B. A., 1992, *Science*, 258, 430
- Burrows, A. & Goshy, J., 1993, *ApJL*, 416, L75
- Burrows, A., Livne, E., Dessart, L., Ott, C. D., & Murphy, J., 2006, *ApJ*, 640, 878
- Burrows, A., Dolence, J. C., & Murphy J. W., 2012, *ApJ*, 759, 5
- Burrows, A., 2013, *Rev. Mod. Phys.*, 85, 245
- Buras, R., Rampp, M., Janka, H.-Th., & Kifonidis, K., 2003, *PRL*, 90, 241101-1
- Couch, S. M., 2013, *ApJ*, 775, 35
- Chevalier, R. A. & Soker, N., 1989, *ApJ*, 341, 867
- Dolence, J. C., Burrows, A., Murphy, J. W., & Nordhaus, J., 2013, *ApJ*, 765, 110
- Fernández, R., & Thompson, C., 2009, *ApJ*, 697, 1827
- Fernández, 2010, *ApJ*, 725, 1563
- Foglizzo, T., Scheck, L., & Janka, H.-Th., 2006, *ApJ*, 652, 1436
- Foglizzo, T., Galletti, P., Scheck, L., & Janka, H.-Th., 2007, *ApJ*, 654, 1006
- Foglizzo, T., 2009, *ApJ*, 694, 820
- Foglizzo, T., Masset, F., Guilet, J., & Durand, G., 2012, *Phys. Rev. Lett.*, 108, 051103
- Fryer, C. L. & Heger, A., 2000, *ApJ*, 541, 1033

- Fryer, C. L. & Warren, M. S., 2002, *ApJ*, 574, L65
- Fryer, C. L. & Warren, M. S., 2004, *ApJ*, 601, 391
- Guilet, J., Sato, J., and Foglizzo, T., 2010, *ApJ*, 713, 1350
- Guilet, J. and Foglizzo, T., 2012, *MNRAS*, 421, 546
- Hanke, F., Marek, A., M’uller, B., & Janka, H.-T., 2012, *ApJ*, 755, 138
- Hanke, F., M’uller, B., Wongwathanarat, A., & Janka, H.-T., 2013, *ApJ*, 770, 66
- Hayes, J. C., Norman, M. L., Fiedler, R. A., Bordner, J. O., Li, P. S., Clark, S. E.,  
ud-Doula, A., & Mac Low, M.-M. 2006, *ApJS*, 165, 188
- Herant, M., Benz, W., & Colgate, S., 1992, *ApJ*, 395, 642
- Heger, A., Langer, N., & Woosley, S. E., 2000, *ApJ*, 528, 368
- Heger, A., Woosley, S. E., & Spruit, H. C., 2005, *ApJ*, 626, 350
- Iwakami, W., Kotake, K., Ohnishi, N., Yamada, S., & Sawada, K., 2008, *ApJ*, 678, 1207
- Iwakami, W., Ohnishi, N., Kotake, K., Yamada, S., & Sawada, K., 2008, *Journal of Physics:*  
*Conference Series*, 112, 042021
- Iwakami, W., Kotake, K., Ohnishi, N., Yamada, S., & Sawada, K., 2009, *ApJ*, 700, 232
- Iwakami, W., Ohnishi, N., Kotake, K., Yamada, S., & Sawada, K., 2009, *Astrophysics and*  
*Space Science*, 322, 43
- Iwakami, W., Nagakura, H., & Yamada, S., 2012, *ArXiv.1308.0829*
- Janka, H.-T., 1996, *Astron. Astrophys.*, 306, 167
- Janka, H.-T., 2012, *Annu. Rev. Nucl. Part. Sci.*, 62, 407

- Kotake, K., Yamada, S. & Sato, K., 2003, *ApJ*, 595, 304
- Leonard, D. C. et al., 2006, *Nature*, 440, 505
- Liebendörfer, M., Rampp, M., Janka, H.-Th., & Mezzacappa, A., 2005, *ApJ*, 620, 840
- Müller, E. & Hillebrandt, W., 1981, *ApJ*, 103, 358
- Murphy, J. W., Dolence, J. C. & Burrows, A., 2013, *ApJ*, 771, 52
- Nordhaus, J., Burrows, A., Almgren, A., & Bell, J., 2010, *ApJ*, 720, 694
- Nakamura, K., Kuroda, T., Takiwaki, T., & Kotake, K., arXiv:1403.7290
- Nagakura, H., Sumiyoshi, K., & Yamada, S., 2014, in preparation.
- Ohnishi, N., Kotake, K., & Yamada, S., 2006, *ApJ*, 641, 1018
- Ott, C. D., Abdikamalov, E., Mösta, P., Haas, R., Drasco, S., O’Connor, E. P., Reisswig, C., Meakin, C. A., & Schnetter, E., 2013, *ApJ*, 768, 2013
- Scheck, L., Janka, H.-Th., Foglizzo, T., & Kifonidis, K., 2008, *A&A*, 477, 931
- Sumiyoshi, K., Yamada, S., Suzuki, H. Shen, H., Chiba, S., & Toki, H., 2005, *ApJ*, 629, 922
- Shen, H., Toki, H., Oyamatsu, K., & Sumiyoshi, K. 1998, *NuPhA*, 637, 435
- Sumiyoshi, K., Takiwaki, T., & Matsufuru, H., 2014, arXiv:1403.4476
- Takiwaki, T., Kotake, K., & Suwa, Y., 2012, *ApJ*, 749, 98
- Tassoul, J.-L., 1978, *Theory of Rotating Stars* (Princeton, NJ: Princeton University Press)
- Wang, L., Howell, A., Höflich, P., & Wheeler, J. C., 2001, *ApJ*, 550, 1030
- Walder, R., Burrows, A., Ott, C. D., Livne, E., Lichtenstadt, I., & Jarrah, M., 2005, *ApJ*, 626, 317

Wongwathanarat, A., Janka, H.-T., & M<sup>’</sup>uller, 2013, A&A, 552, A126

Yamada, S. & Sato, K., 1990, ApJ, 358, L9

Yamada, S. & Sato, K., 1991, ApJ, 382, 594

Yamada, S. & Sato, K., 1994, ApJ, 434, 268

Yamasaki, T., & Yamada, S., 2005, ApJ, 623, 1000

Yamasaki, T., & Yamada, S., 2006, ApJ, 650, 291

Yamasaki, T., & Yamada, S., 2007, ApJ, 656, 1019

Yamasaki, T., & Foglizzo, T., 2008, ApJ, 679, 607

Table 1. Summary of parameters for all models.

| Model | $\dot{M}^a$                | $L_\nu^b$                      | $r_{\text{in}}^c$ | $r_{\text{out}}^d$ | Flow Patterns             | $\beta_{\text{exp}}^e$ |
|-------|----------------------------|--------------------------------|-------------------|--------------------|---------------------------|------------------------|
|       | $[M_\odot \text{ s}^{-1}]$ | $[10^{52} \text{ erg s}^{-1}]$ | [km]              | [km]               | (Nonlinear, $\beta = 0$ ) |                        |
| A     | 0.2                        | 2.5                            | 33                | 655                | SPB                       | 1.0                    |
| B     | 0.2                        | 2.75                           | 34                | 688                | BB                        | 0.8                    |
| C     | 0.2                        | 3.0                            | 36                | 712                | BB                        | 0.0                    |
| D     | 0.6                        | 4.0                            | 41                | 822                | SP                        | 0.9                    |
| E     | 0.6                        | 4.5                            | 44                | 872                | BB                        | 0.4                    |
| F     | 0.6                        | 5.0                            | 46                | 920                | BB                        | 0.0                    |
| G     | 1.0                        | 5.0                            | 46                | 919                | SP                        | 0.9                    |
| H     | 1.0                        | 5.5                            | 49                | 965                | SPP                       | 0.5                    |
| I     | 1.0                        | 6.0                            | 51                | 1007               | SP                        | 0.0                    |

<sup>a</sup>Mass accretion rate.

<sup>b</sup>Neutrino luminosity.

<sup>c</sup>Radius of the inner boundary.

<sup>d</sup>Radius of the outer boundary.

<sup>e</sup>Critical value of the normalized specific angular momentum.

Note. — Flow patterns are classified into sloshing motion (SL), spiral motion (SP), buoyant bubbles (BB), spiral motion with rising buoyant bubbles (SPB), and spiral motion with pulsating rotational velocity (SPP).

Table 2. Flow patterns and physical parameters for models B.

| Model | Semi-Nonlinear | $\chi^a$       | $r_{\text{gain}}^b$ | $r_{\text{sh}}^c$ | Nonlinear | $\bar{\chi}^d$   | $\bar{r}_{\text{gain}}^e$ | $\bar{r}_{\text{sh}}^f$ | $\bar{A}_{l=1,2}/\bar{A}_{l=4,5}^g$ |
|-------|----------------|----------------|---------------------|-------------------|-----------|------------------|---------------------------|-------------------------|-------------------------------------|
|       | pattern        | (initial flow) | [km]                | [km]              | pattern   | (nonlinear flow) | [km]                      | [km]                    |                                     |
| B0-3  | SP/BB          | 4.1            | 60                  | 99                | BB        | 5.0-5.1          | 57                        | 133-136                 | 2.2-2.4                             |
| B4    | BB             | 4.1            | 60                  | 99                | BB        | 5.1              | 56                        | 139                     | 1.7                                 |
| B5    | SP             | 4.1            | 60                  | 99                | BB        | 5.0              | 56                        | 132                     | 1.5                                 |

<sup>a</sup> $\chi$  parameter in the initial flow

<sup>b</sup>Radius of the boundary between the heating and cooling regions in the initial flow

<sup>c</sup>Radius of the shock wave in the initial flow

<sup>d</sup> $\chi$  parameter in the time- and angle-averaged flow

<sup>e</sup>Radius of the boundary between the heating and cooling regions in the time- and angle-averaged flow

<sup>f</sup>Radius of the shock wave in the time- and angle-averaged flow

<sup>g</sup>The ratio of the time-averaged mode amplitudes of  $A_{l=1,2}$  to  $A_{l=4,5}$

Note. — Models B0-3, B4, and B5 correspond to the normal, middle, and high resolution models. The grid points of normal, middle, and high resolution models are  $300 \times 30 \times 60$ ,  $300 \times 50 \times 100$ , and  $300 \times 60 \times 120$ , respectively. In the column of the normal resolution models, the ranges of the parameters are listed in the table.



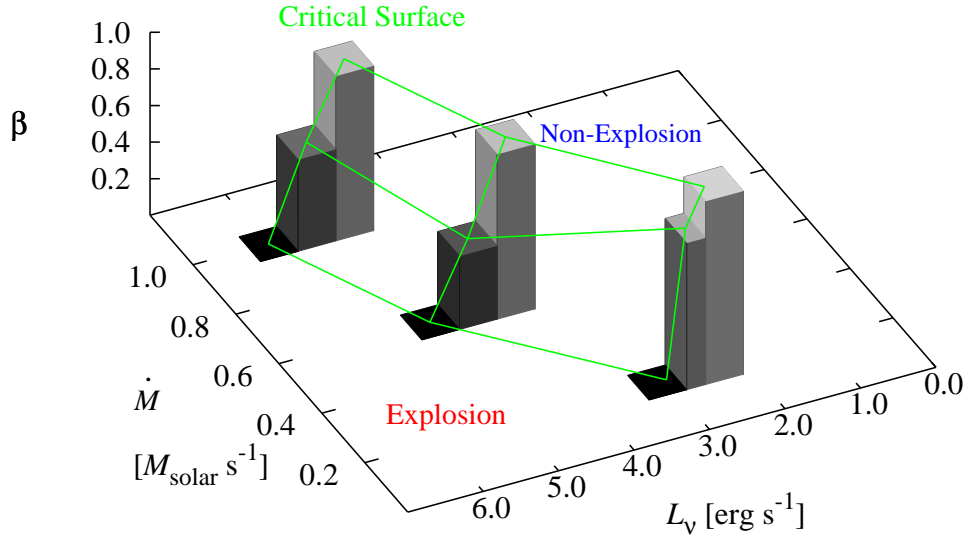


Fig. 1.— The critical surface for explosion as functions of the mass accretion rate  $\dot{M}$ , the neutrino luminosity  $L_{\nu}$ , and the normalized specific angular momentum  $\beta$ . The critical surface is depicted with green lines. The front side of the critical surface corresponds to the explosion region, and the other side agrees with the non-explosion region. The height and color of vertical bars indicate the critical values of the normalized specific angular momentum  $\beta_{\text{exp}}$ .

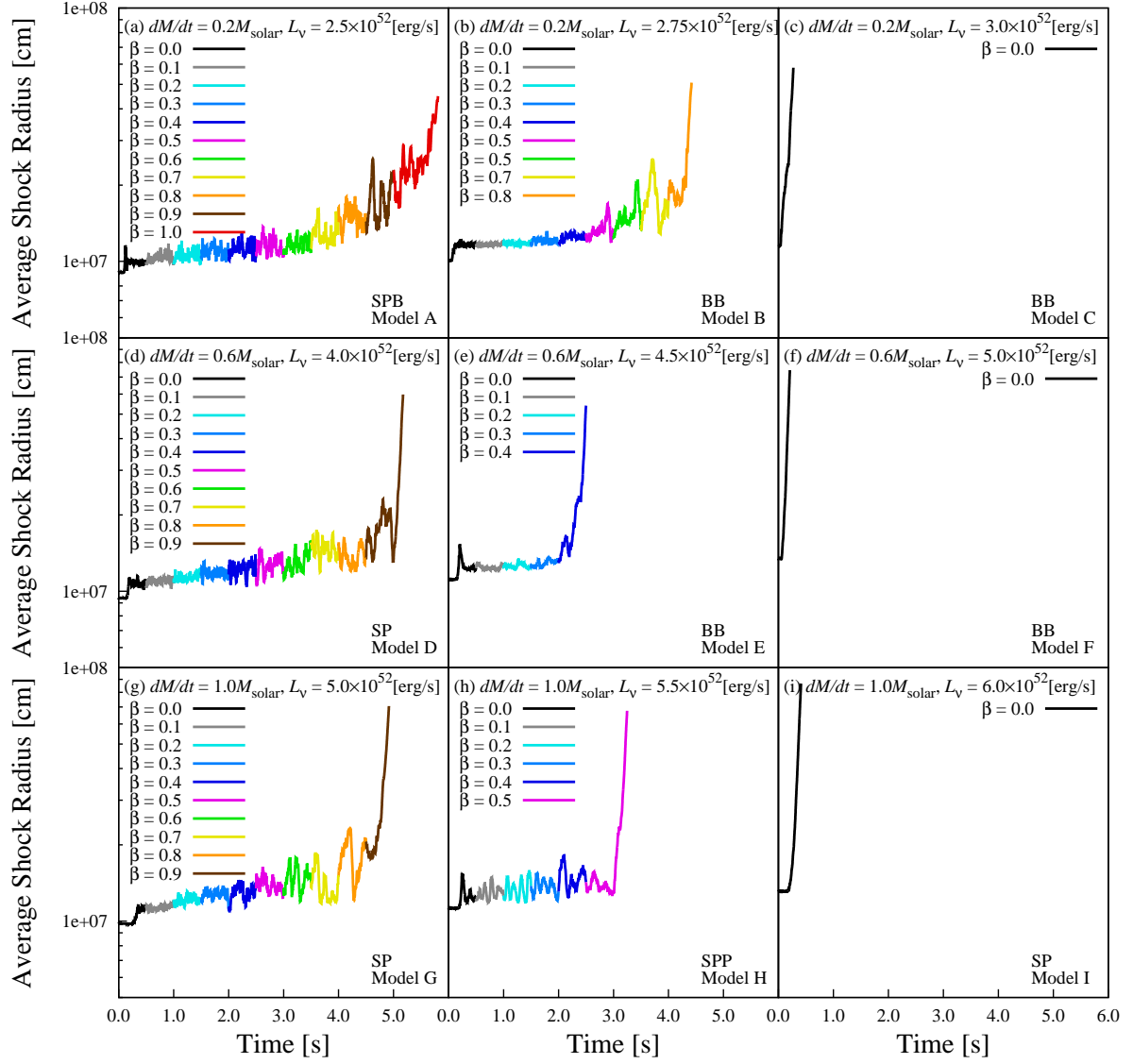


Fig. 2.— Time evolutions of the averaged shock radius with increasing  $\beta$  every 500 ms.

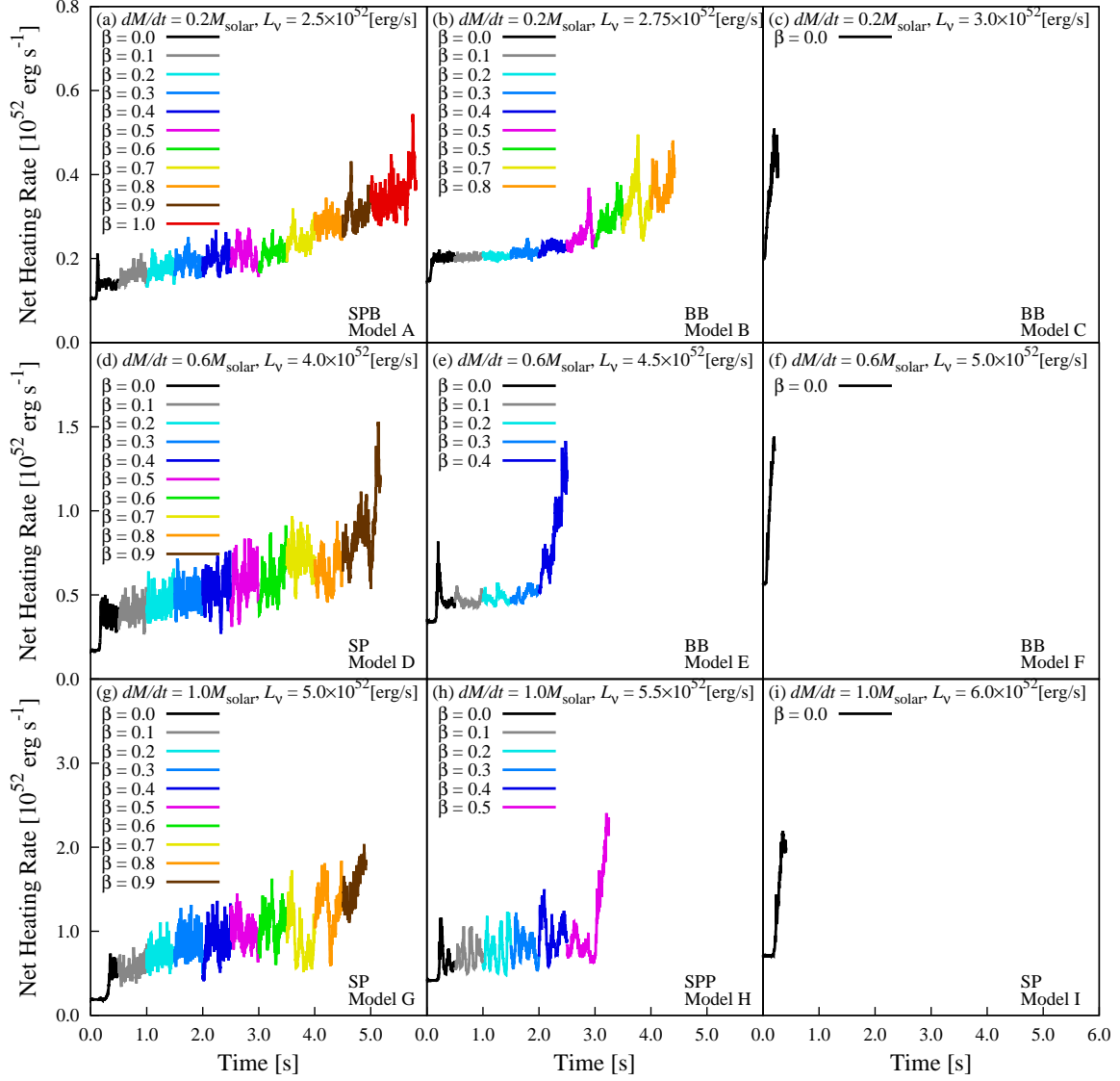


Fig. 3.— Time evolutions of the net heating rate, integrated behind the shock wave, with increasing  $\beta$  every 500 ms.

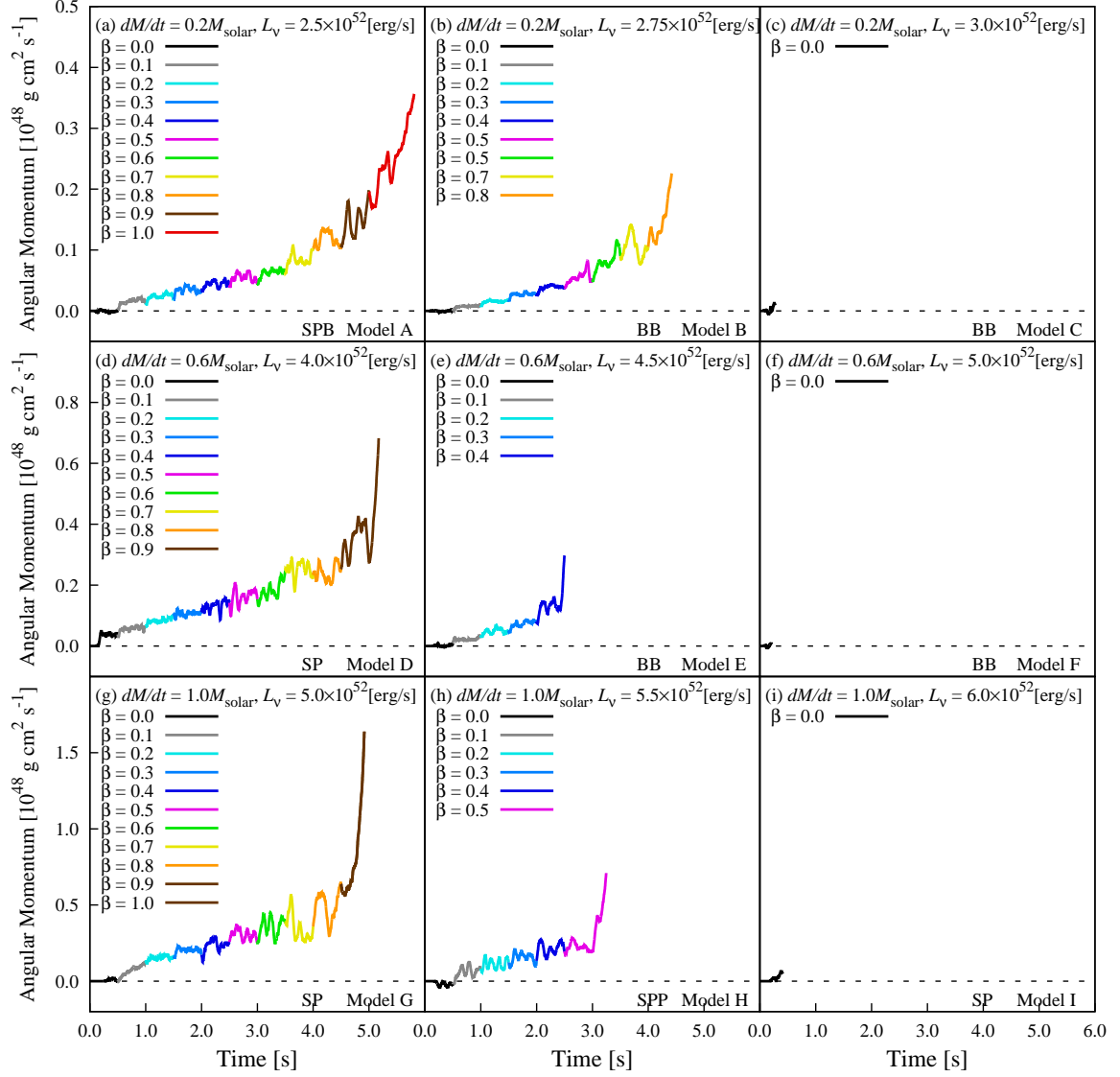


Fig. 4.— Time evolutions of the angular momentum in the polar direction, integrated behind the shock wave, with increasing  $\beta$  every 500 ms.

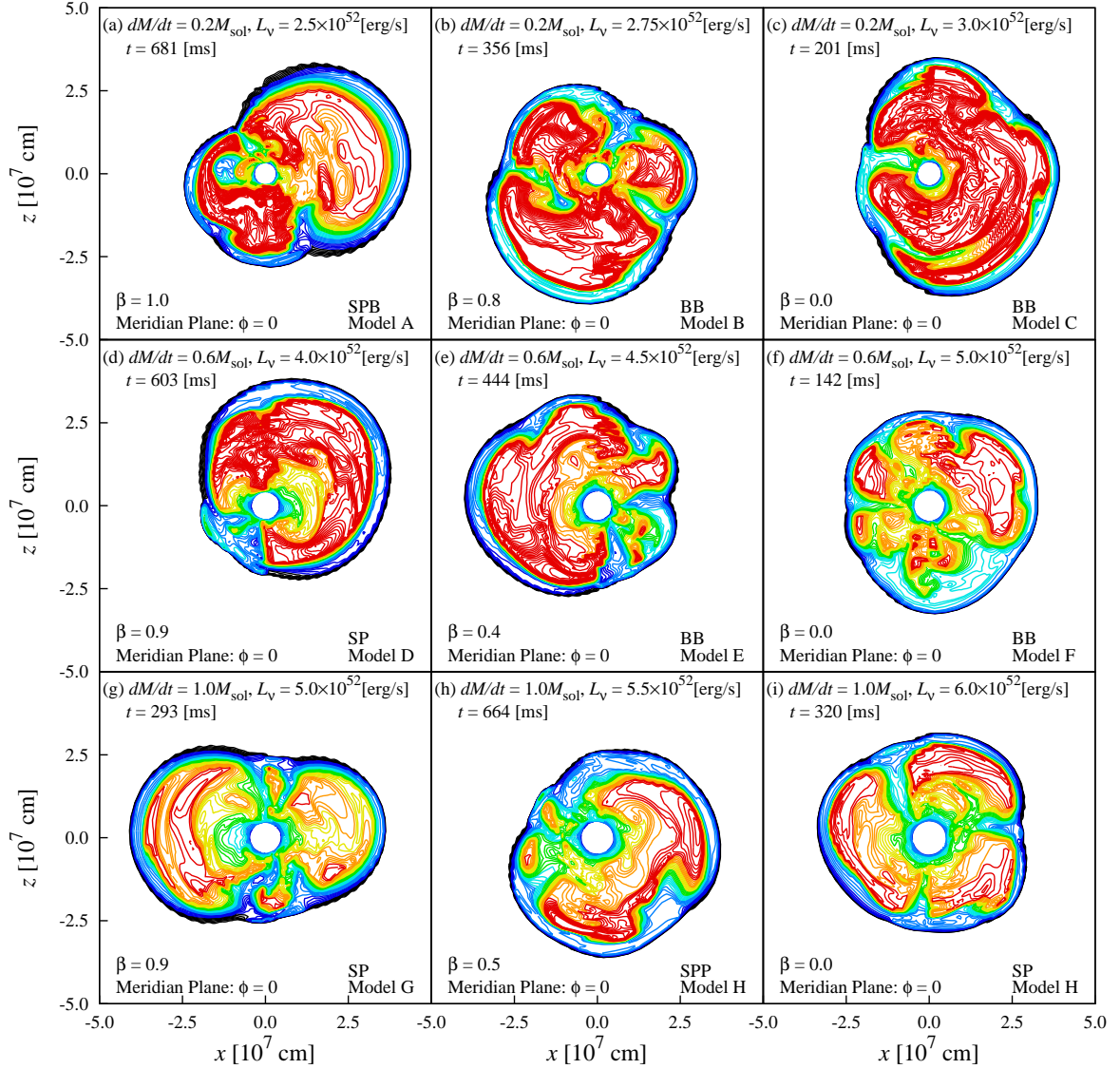


Fig. 5.— Snapshots of the entropy contour map in the meridian plane at  $\phi = 0$  for all models just after the shock revival. The entropy  $S$  is in units of Boltzmann’s constant  $k_b$  per nucleon. The contour levels are in the range of  $4 \leq S \leq 26$  with the increment of  $\Delta S = 0.4$ . The contour lines of higher values are drawn in reddish colors, and those of lower ones are done in bluish colors. The innermost and outermost contour lines agree with the surfaces of the proto-neutron star and the shock wave, respectively.

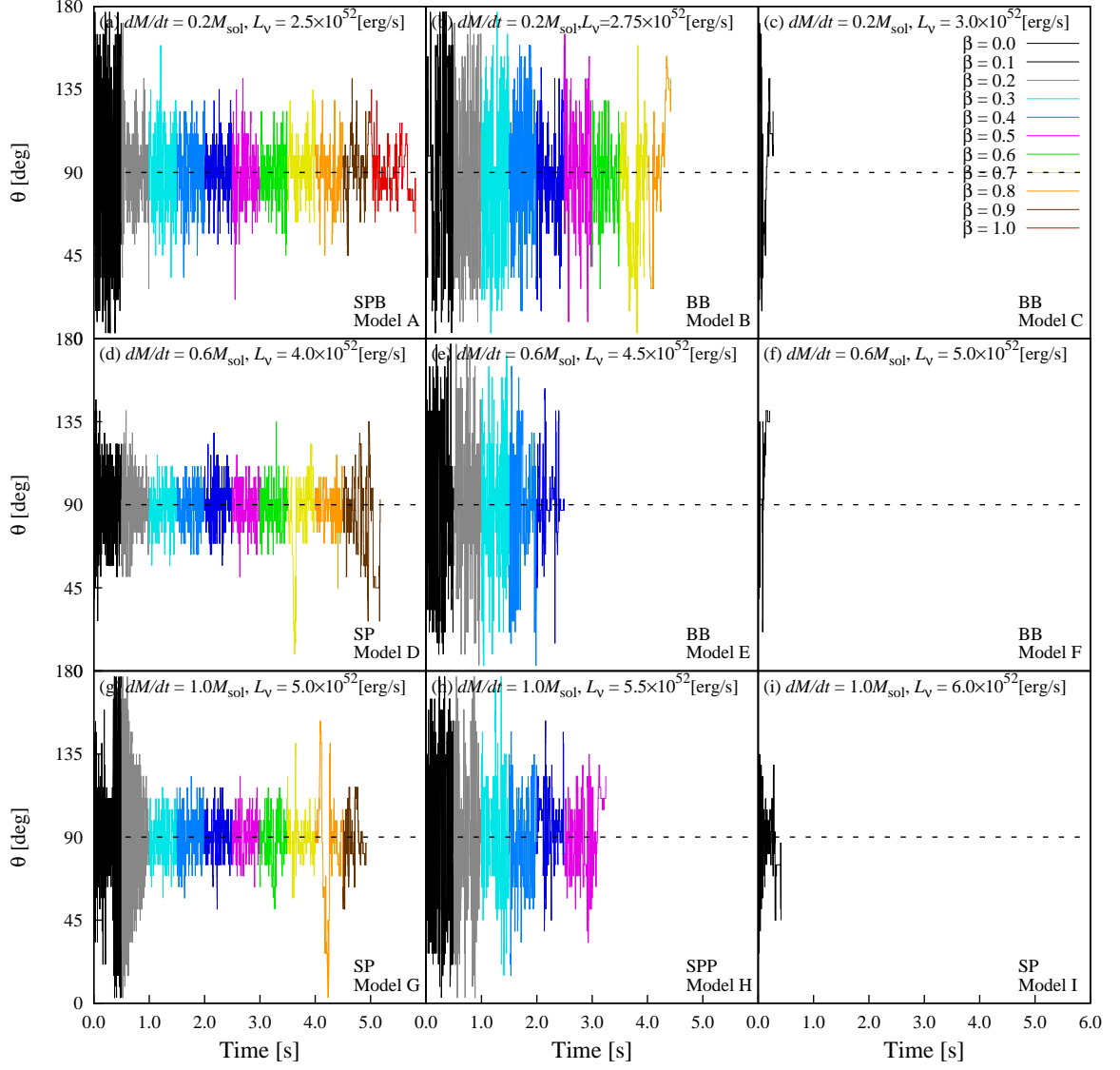


Fig. 6.— Time evolutions of the orientation of the maximum shock radius with increasing  $\beta$  every 500 ms. The polar angle  $\theta$  indicating the orientation, are the spherical coordinates.

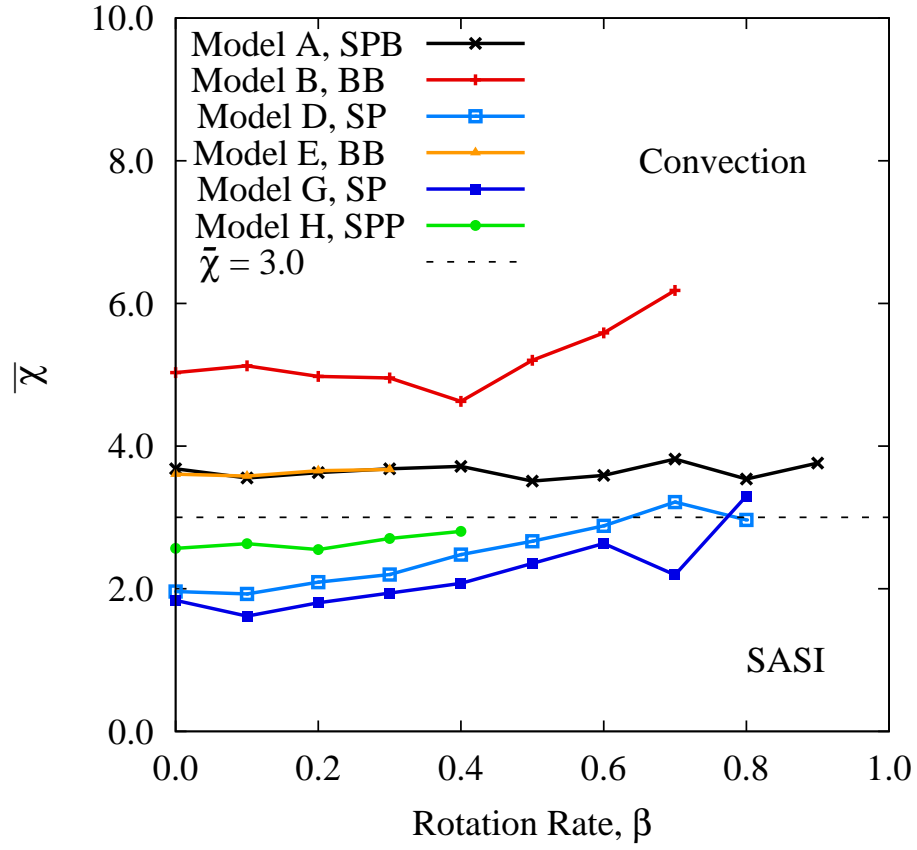


Fig. 7.— The  $\bar{\chi}$  parameter as a function of  $\beta$  for non exploding models.

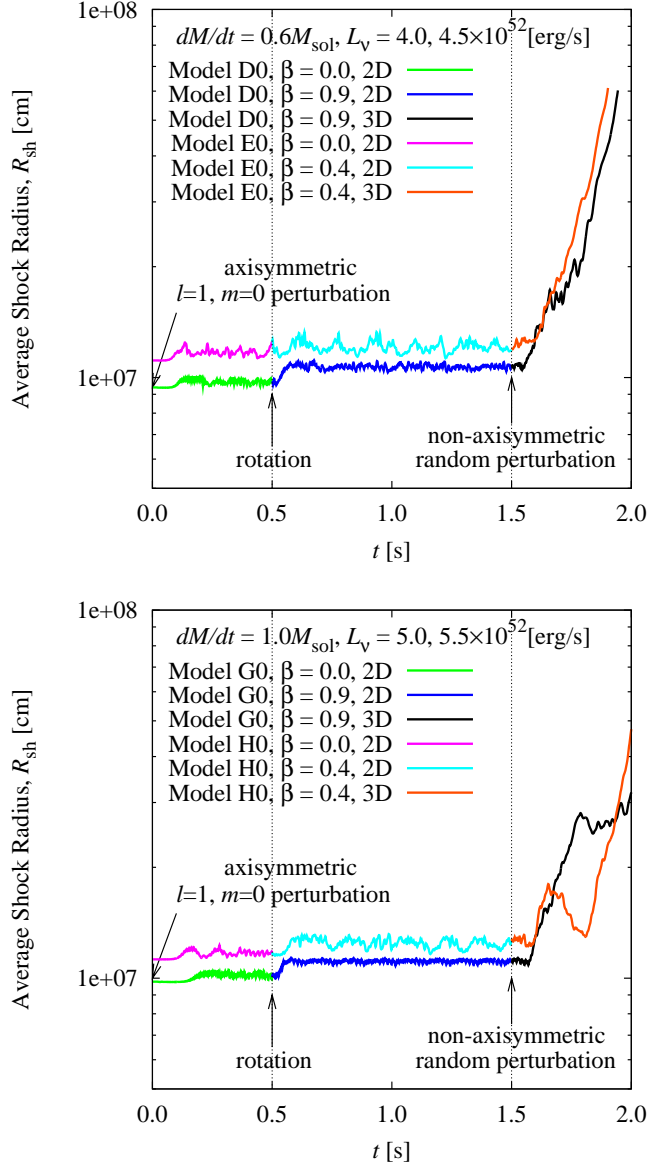


Fig. 8.— Time evolutions of the averaged shock radius for  $\dot{M} = 0.6 M_{\odot}$  (upper panel) and  $\dot{M} = 1.0 M_{\odot}$  (lower panel). Initially, the  $l = 1, m = 0$  perturbation is imposed on the spherically symmetric flow at  $t = 0$ , and the 2D models without rotation are obtained from  $t = 0.0$  to  $0.5$ . Next, the rotating matter is inleted from the outer boundary into the 2D flows at  $t = 0.5$ , and the 2D models with rotation is obtained from  $t = 0.5$  to  $1.5$ . Finally, the non-axisymmetric random perturbation is added to the 2D flows with rotation, and the 3D rotation models can explode.



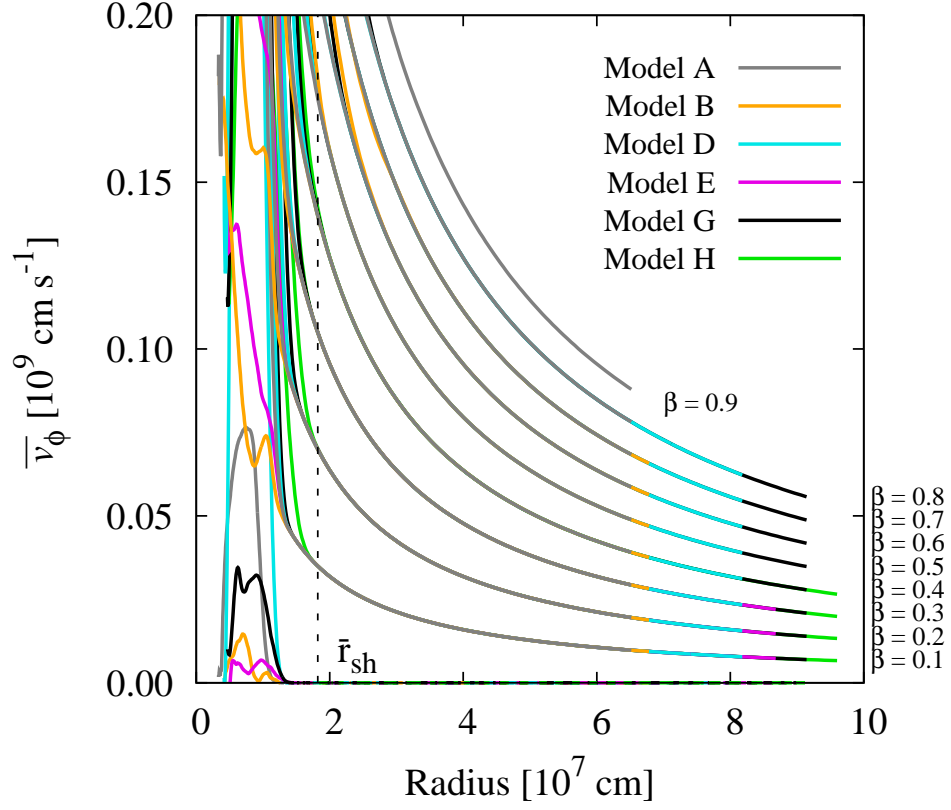


Fig. 9.— The radial distributions of the time- and angle-averaged azimuthal velocity  $\bar{v}_\phi$  for the non-explosion models. The dashed line at  $\bar{r}_{\text{sh}}$  means the maximum radius of the shock wave of all models. The locations of the right endpoints of the lines correspond to the outer boundaries, respectively.

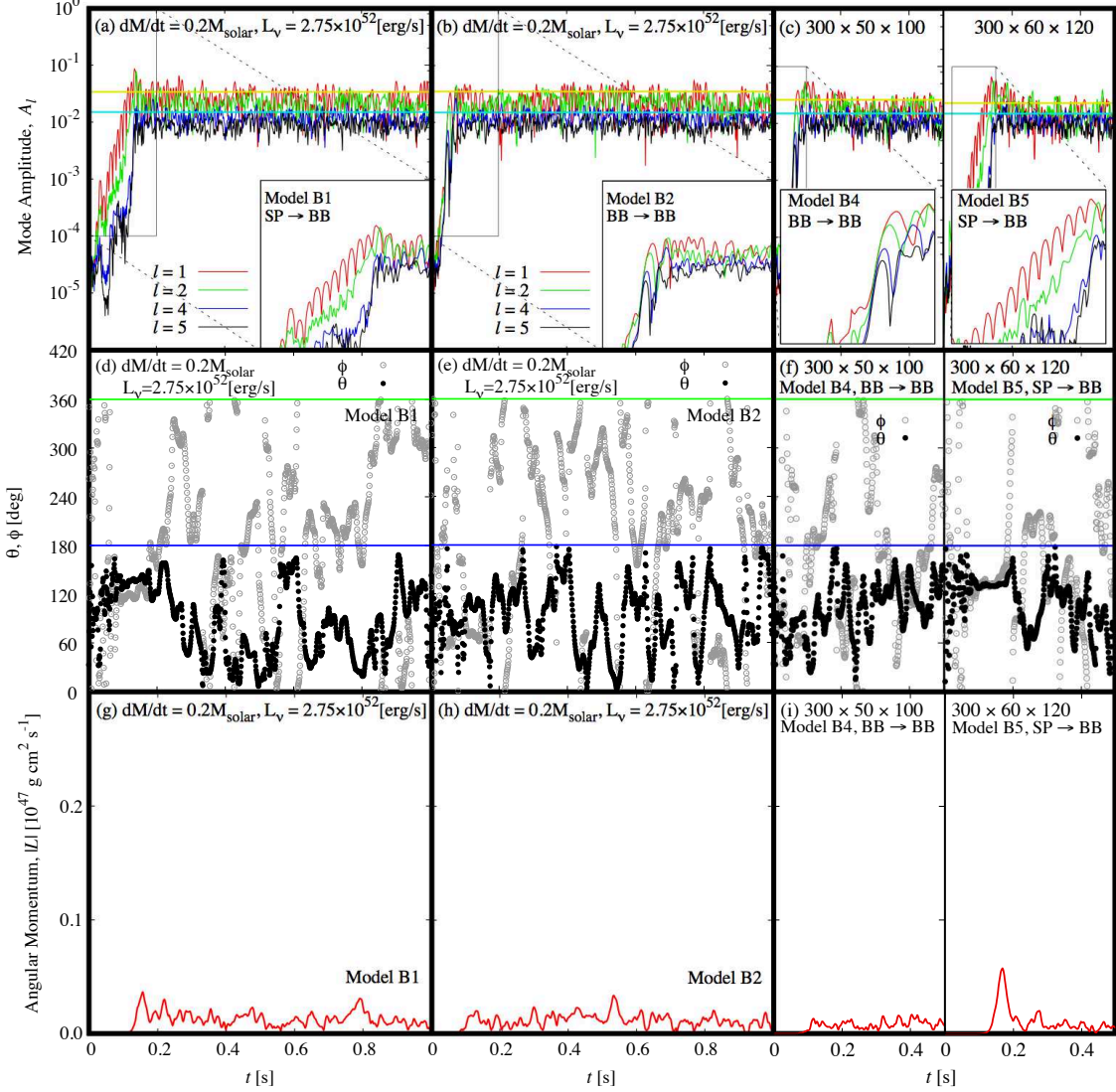


Fig. 10.— Time evolutions of the normalized mode amplitudes, the orientations of the rotation axis, and the magnitudes of angular momentum for Models B1, B2, B4 and B5. In the figures (c), (f) and (i), the left and right panels show the results of  $30 \times 50 \times 100$  and  $30 \times 60 \times 120$  mesh points, respectively. In the figures (a), (b) and (c), the yellow lines correspond to the combined mode amplitudes of  $l = 1, 2$  averaged in the nonlinear phase, whereas the blue lines stand for those of  $l = 4, 5$ , and the insets are the zoom-ups of the indicated portions. In the figures (d), (e) and (f), the angles  $\theta$  (black filled-circle) and  $\phi$  (gray open-circle) indicating the orientation, are the spherical coordinates, and the blue and green lines correspond to  $\pi$  and  $2\pi$ , respectively.